The trade-off of light trapping between top and bottom cell in micromorph tandem solar cells with sputtering ZnO:Al glass substrate

Lisha Bai, Bofei Liu, Jun Fan, Dekun Zhang, Changchun Wei, Jian Sun, Ying Zhao, Xiaodan Zhang*

Institute of Photo Electronics Thin Film Devices and Technology of Nankai University, Key Laboratory of Photoelectronic Thin Film Devices and Technology, Tianjin 300071, PR China

HIGHLIGHTS

- A trade-off between the light response of the top and bottom cell is achieved.
- The light control mechanism was identified through experimentation and simulation.
- A finely textured SnO$_2$:F substrate enhances short-wavelength light coupling.
- A coarsely textured ZnO:Al substrate improves long-wavelength light scattering.
- An n-type μc-SiO$_x$ intermediate reflector can improve the J_{sc} of the top cell.

ARTICLE INFO

ABSTRACT

A simulated and experimental investigation of the trade-off between light trapping and current matching in p-i-n structured a-Si:H/μc-Si:H tandem solar cells is presented, which aims to address the limited short circuit current density (J_{sc}) that results from the low long-wavelength light scattering of the fluorine-doped tin oxide (SnO$_2$:F) substrates typically used. To this end, the mismatch of the J_{sc} between the top and bottom cells is reduced by utilizing a ZnO:Al substrate with optimized long-wavelength light scattering properties as the front contact, thereby improving the response of the bottom cell at the expense of the lower top cell's J_{sc} yet. A trade-off between the top and bottom cell's light response is subsequently found with SnO$_2$ or ZnO:Al as a substrate, by introducing an n-type μc-SiO$_x$ intermediate reflector (IR) between the two component cells. An initial efficiency based on an approximate current matching of 11.90% is achieved for a-Si:H/μc-Si:H tandem solar cell by adopting a magnetron-sputtered and texture-etched ZnO:Al substrate and an optimized n-type μc-SiO$_x$ IR.

1. Introduction

Multi-junction solar cells, composed of an a-Si:H top cell and μc-Si:H bottom cell, can in principle utilize the spectrum of irradiated solar energy more effectively than traditional single-junction thin-film silicon solar cells. However, improving the efficiency of tandem solar cells presents a big challenge due to the difficulty in achieving an ideal short-circuit current density (J_{sc}) matching between the two sub-cells. Since the J_{sc} of the overall cell is determined by the lesser of the two sub-cells, any mismatch can therefore significantly reduce the efficiency of tandem solar cells.

Effective light trapping is an essential requirement for the design of thin-film solar cells [1,2], as this can increase the optical path length of the incident light and enhance the absorption of the intrinsic layer. This has led to the development of solar cells with a greater optical thickness and lower electrical thickness, thereby mitigating the Staebler-Wronski (SW) effect on the solar cell's performance and reducing the production cost. The relative success in this area has driven the search for a suitable light trapping structure to facilitate a matching of J_{sc} between two sub-cells in a multi-junction solar cell. From this, it has been found that using a textured layer of a transparent conductive oxide (TCO) as the front contact can improve the light trapping of the microcrystalline silicon bottom cell, as well as reduce the required thickness of the absorber layer.

Currently, the most widespread TCO materials are tin oxide (SnO$_2$), indium–tin oxide (ITO) and zinc oxide (ZnO), all of which

* Corresponding author. Tel./fax: +86 22 23502778.
  E-mail address: xdzhang@nankai.edu.cn (X. Zhang).

have been well-studied in an effort to improve their optical and electrical properties. The surface morphology, which can be characterized by the root mean square (RMS) roughness and the correlation length (δ_{rms}, l_c), determines the light scattering properties. The range and intensity of the response spectrum can be modulated by the surface morphology with proper (δ_{rms}, l_c).

The effect of the SW effect on tandem solar cells can also be minimized by the use of a thinner top cell. For increasing the J_{sc} of the a-Si:H top cell without compromising its stability, an IR can be integrated to adjust the current matching apart from varying the thicknesses of the two absorber layers [3–5].

In this paper, the performance of a-Si:H/μc-Si:H tandem solar cells deposited on commercial SnO$_2$:F substrates is reported first of all. In this, the problems that are normally encountered with SnO$_2$:F substrates are addressed by the introduction of an alternative magnetron-sputtered and texture-etched ZnO:Al substrate. Then we conduct the surface morphology of the wet-etched ZnO:Al and SnO$_2$:F analysis and evaluate the light scattering properties of the corresponding morphology. Finally, an a-Si:H/μc-Si:H tandem solar cell incorporating both this new substrate and an IR between the two component cells is fabricated and its performance evaluated.

2. Experimental

A-Si:H absorber layers and n-μc-SiO$_x$:H films were deposited by radio frequency plasma enhanced chemical vapor deposition (RF-PECVD); with μc-Si:H layers being deposited by very high frequency plasma enhanced chemical vapor deposition (VHF-PECVD) [6,7]. A mix of H$_2$ and SiH$_4$ was used as a source gas for depositing the intrinsic layer of a-Si:H and μc-Si:H, and the substrate temperature and chamber pressure were carefully controlled to ensure that the experimental conditions were the same for all samples. Magnetron-sputtered ZnO:Al substrates were etched for 40 s in 0.5% diluted hydrochloric acid (HCl) solution to produce randomly-textured surfaces. Tandem a-Si:H/μc-Si:H solar cells were then fabricated onto the texture-etched ZnO:Al substrates, and APCVD-grown SnO$_2$:F, under the same condition. The resulting cells had an area of 0.253 cm^2, with an a-Si:H and μc-Si:H absorber layer thickness of around 280 nm and 2000 nm, respectively.

The $I-V$ characteristics of the samples from which we obtained the V_{oc} and the FF, were measured under a 1-Sun (AM 1.5, 25 °C, 100 mWcm^{-2}) using a Wacom WXs-156s-l2 dual-beam solar simulator. This provided an excellent simulation of the AM 1.5 spectrum through a calibrated superposition of the simulator's two filtered light sources. External quantum efficiency (EQE) curves of these cells were obtained by quantum efficiency measurement, and used to characterize the response at different wavelengths. The J_{sc} values were calculated from EQE curves by integrating the response across the entire wavelength range.

3. Results and discussion

3.1. SnO$_2$-based tandem solar cells

Ideally, the front electrode of a p-i-n solar cell should have a sheet resistance (R_{sq}) of no more than ~10Ω [8]; while at the same time, its average absorption between 400 and 1100 nm should be below ~6–7% [8]. An appropriate quantitative measure of the quality of TCOs can also be characterized with the figure of merit, which can be acquired by the ratio of the electrical conductivity σ to the visible absorption coefficient α [9]

$$\frac{\sigma}{\alpha} = -\{R_S \ln(T + R)\}^{-1}$$

where R_s means the sheet resistance in ohms per square, T the total visible transmission, and R the total visible reflectance. Thus a larger σ/α indicates better transparency with a lower resistance for the transparent conductor.

At present, SnO$_2$:F [10] is one kind of substrate that comes close to fulfilling these requirements (the figure of merit σ/α is about 2.5), and is not surprisingly therefore the most widely used in commercial solar cells [11]. With this in mind, p-i-n type a-Si:H/μc-Si:H tandem solar cells were fabricated, incorporating APCVD-grown SnO$_2$:F as the front TCO film.

The EQE curves for this cell's respective components, as well as its overall performance, are shown in Fig. 1. From this, the J_{sc} of the top cell is 12.28 mA cm^{-2}, whereas the bottom cell has a value of 10.93 mA cm^{-2}. This mismatch between the two subcells can be seen to limit the J_{sc} of the tandem cell, which is typical of a SnO$_2$ substrate. To reduce this mismatch, there are two methods that can be considered: increasing the thickness of the bottom cell, though this may decrease the V_{oc} [12]; or finding a more efficient means of light trapping for the bottom cell, which can enhance long-wavelength light scattering.

3.2. Light trapping of microcrystalline silicon bottom cell

3.2.1. Surface morphology of APCVD-grown SnO$_2$:F and sputtered ZnO:Al

To increase J_{sc} of the bottom cell, a high-quality magnetron-sputtered and texture-etched ZnO:Al substrate, which is in-house developed in our laboratory and shows the figure of merit of 5.1, was introduced: Fig. 2 showing two-dimensional (2D) AFM images and surface profiles of both the ZnO:Al and APCVD-grown SnO$_2$:F (Asahi type U) substrates used.

It is obviously shown that the surface morphology of the ZnO:Al is smooth with large periodicity and it's clear that crater-like features appear on the surfaces of ZnO:Al. In contrast, the surface of SnO$_2$ is defined by sharp pyramids with a much finer texture, its RMS roughness (δ_{rms} = 35 nm) being significantly less than that of ZnO:Al (δ_{rms} = 164 nm).

Since the RMS represents the average longitudinal depth, it is also important to consider the correlation length (l_c) of the two TCOs which gives a measure of the average lateral feature sizes of the TCOs surface morphology [13] by fitting the one-dimensional
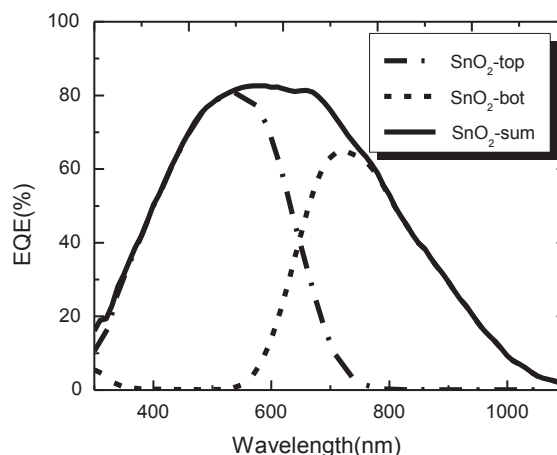

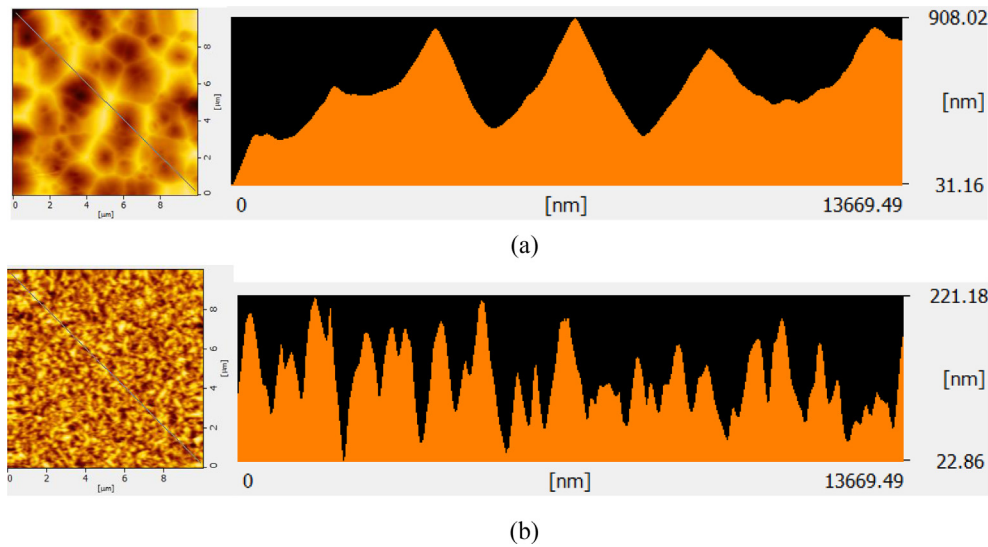**Fig. 1.** EQE curves of a-Si:H/μc-Si:H tandem cell on a SnO$_2$ substrate.

Fig. 2. 2D AFM images and surface profiles (gray line) for a 10×10 μm^2 scan area of: (a) magnetron-sputtered and texture-etched ZnO:Al, and (b) APCVD-grown SnO$_2$:F.

auto-correlation function (ACF$_{1D}$) with the Gaussian function. In this way, the l_c of SnO$_2$ and ZnO:Al were found to be 200 and 748 nm, respectively. Therefore, the surface of SnO$_2$ is both shallower and laterally smaller. Surface profiles are also shown in Fig. 2, in which we can see obviously the average feature size of SnO$_2$ (around 200 nm lateral, 100 nm in height) is significantly smaller than that of ZnO:Al (1500 nm lateral, 500 nm in height).

Fig. 3 shows power spectral density (PSD) profiles for the ZnO:Al and SnO$_2$ substrates, as calculated by applying a Fast Fourier transform (FFT) to the ACF$_{2D}$ function obtained from AFM scans [14]. The PSD characterizes the distribution of surface features with different lateral sizes [15]. When the lateral size of surface features can be comparable to the effective wavelength ($\lambda_{eff} = \lambda_{vac}/n_{TCO}$), the scattering intensity of the incoming light will be most efficiently [16].

Region I is defined by the presence of nano-features with dimensions of 20–70 nm (half the effective wavelength $\lambda/(2n)$) that act as an effective refractive index gradient, thereby reducing reflection and ensuring that more light is coupled into the solar cell in this interface [16]. In contrast, Region II exhibits much greater dimensions, which are directly related to its long-wavelength scattering characteristics. Hence, the larger PSD of Region I in

SnO$_2$ indicates that its surface is defined predominantly by nanoscale features. Conversely, the higher PSD of ZnO:Al in Region II confirms the much larger size of its surface features.

3.2.2. Light scattering of APCVD-grown SnO$_2$:F and sputtered ZnO:Al

In order to further understand the differences in surface morphology and reflection identified in the PSD profiles, the haze spectrum was determined from the total optical transmission Tt(λ) and specular transmission Ts(λ) of the TCOs and angular intensity distribution (AID) was calculated. As shown in Fig. 4, the transmittance of ZnO:Al is substantially zero at wavelengths of less than 330 nm (cutoff wavelength). The optical band gap determines the cutoff wavelength, and the energy of light with wavelengths less than 330 nm is greater than ZnO:Al's optical band gap, therefore the transmittance decreases to zero. Consequently, the transmittance of SnO$_2$:F at wavelengths less than 390 nm is higher, due to its larger optical band gap. Nevertheless, ZnO:Al still has a superior total transmittance within the more usable region of the visible light spectrum, which is comparable to that of the ZnO:Al fabricated by LG Electronics Advanced Research Institute (LGE) on
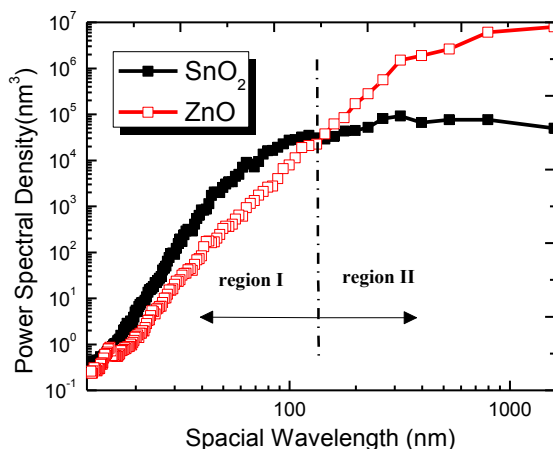

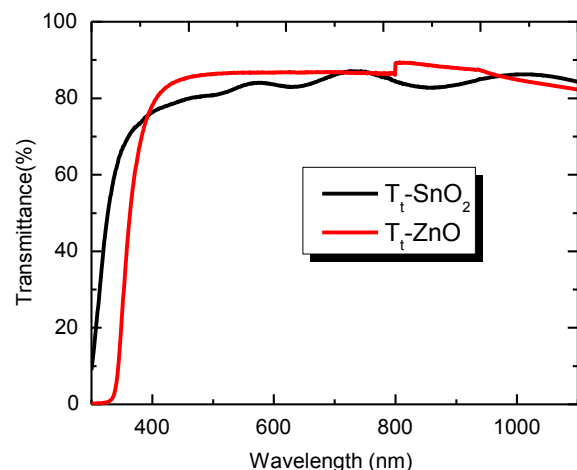**Fig. 3.** Power spectral density profiles of different TCOs.

Fig. 4. Total transmission of glass/ZnO:Al, and glass/SnO$_2$:F architectures.

which a world-record initial efficiency of 16.1% for PIN type triple junction solar cells has been achieved [17]. Moreover, the smaller RMS of SnO_2:F results in an interference pattern exists in the transmittance curve.

To determine the effect of the surface feature size on light scattering, the 2D AID were calculated as a function of the scattering angle ($0°−90°$) and wavelength ($350−1100$ nm) using a simulated structure of air/glass/TCO/air. This calculation was based on a scalar scattering theory suitable for estimating the scattering properties of nano-textured interfaces [18]. By applying a 2D Fourier transform to $G_T(x,y)$ pupil function [18], which is related to the surface morphology $z(x,y)$, the materials n_1 and n_2 forming the rough interface and determined by:

$$G_T(x,y) = \sqrt{\frac{T}{A}} \exp(ik_0 z(x,y)(n_1 - n_2))$$

the field in k-space $U_T(k)$ can be determined; thus, the angular intensity distribution at a certain angle, AID(θ), can be obtained by following formula [18]:

$$AID_T(\theta) = \frac{K_0 n_{2,1}}{2\pi \sin\theta} \oint_c |U_T(K)|^2 \cos\theta \, ds$$

At the same time, the haze in transmission can also be estimated by Ref. [18,19]

$$H_T(\lambda) = \frac{\sum_{k_x^2+k_y^2 \leq k_0^2 n_{2,1}^2} |U_T(k_x, k_y)|^2 - |U_T(0,0)|^2}{\sum_{k_x^2+k_y^2 \leq k_0^2 n_{2,1}^2} |U_T(k_x, k_y)|^2}$$

This calculation provides a precise determination of the extent of light scattering versus the scattering angles and wavelengths, and therefore gives a deeper understanding of the light scattering behavior after the light penetrates the scattering interface. The refractive indexes for SnO_2 and ZnO materials used in this calculation were obtained from literature values [20].

Fig. 5a and b shows the scattering angles of SnO_2:F and ZnO:Al, in which it is clearly shown that the scattering angle of ZnO:Al concentrates within a small angle range across the entire spectral range, and with the increase of wavelength, the scattering angle slightly diverges. Conversely, the scattering angle of SnO_2:F distributes wider and it becomes more divergent when the wavelength increases. We therefore selected to compare the angular intensity distribution at a fixed wavelength of 800 nm, so as to provide an effective characterization of the long-wavelength light absorption of microcrystalline silicon bottom cells. As shown in Fig. 5c, the intensity of ZnO:Al in region I is larger than SnO_2:F, but smaller in Region II, an observation that is supported by the grating equation [21]

$$P \cdot n \cdot \sin(\theta_m) = m \cdot \lambda$$

where P is the grating period of the substrate which approximates the correlation length, n is the refractive index of the propagating media after diffraction, m denotes the diffraction order and θ_m specifies the diffraction angle. This demonstrates that for a given period, the diffraction angle is directly proportional to the incident wavelength; and therefore, any increase in wavelength increases the diffraction angle (as shown in Fig. 5a,b). It also means the larger grating period of ZnO:Al that was identified in Fig. 2 can explain the more divergent scattering angle of SnO_2:F with increasing wavelength. In addition, by comparing the angular intensity distribution at 800 nm in Fig. 5(c), it is apparent that the concentrating of the angular intensity of ZnO:Al within a small angular range is due to the
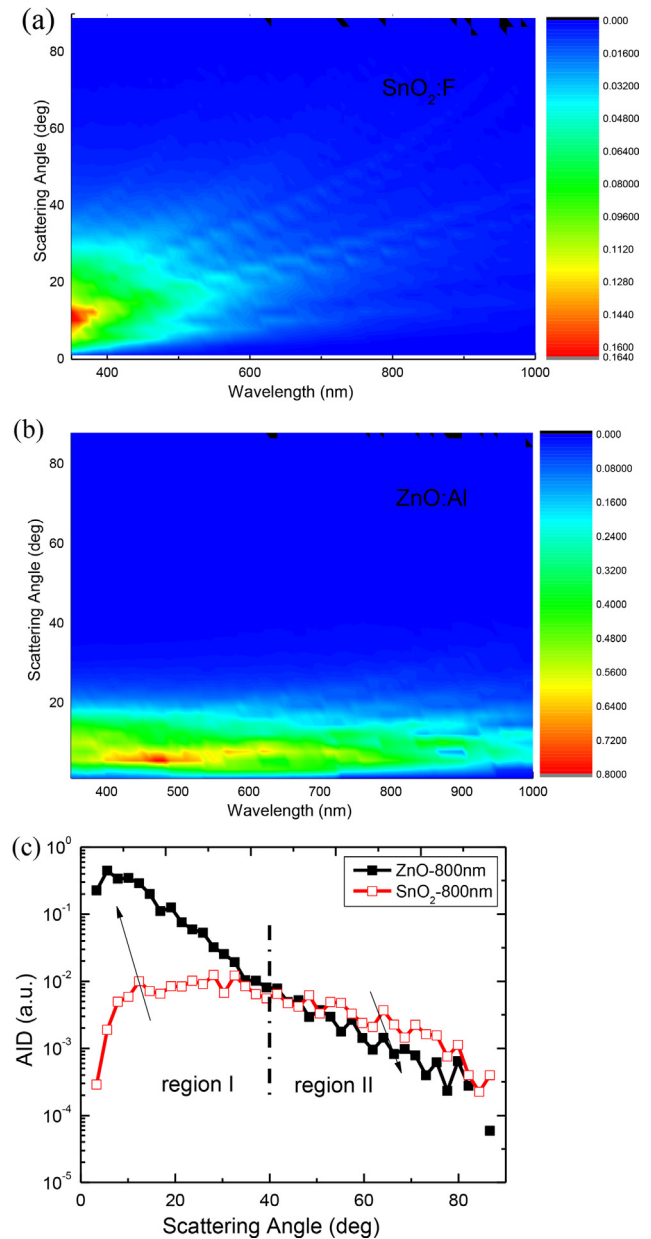

Fig. 5. 2D angular intensity distribution of (a) SnO_2:F and (b) ZnO:Al as a function of wavelengths and scattering angles. (c) Angular intensity distribution of SnO_2:F and ZnO:Al at a wavelength of 800 nm.

reduction in diffraction angle θ_m with increasing period. It is disadvantageous to maximize the light path in the intrinsic layer.

The haze value represents the scattering intensity of an interface with a certain morphology. In the simulated and measured haze value of glass/ZnO:Al and glass/SnO_2:F shown in Fig. 6, it is obvious that the haze of ZnO:Al is much greater than SnO_2:F across the entire spectral range, but decreases with wavelength. Additionally, a higher haze ratio of 68% at a typical wavelength of 850 nm, which is greater than that of LGE's (48%) [17], illustrates our in-house fabricated ZnO:Al films' excellent optical properties. Consequently, even though the scattering angle of ZnO:Al is limited to small angles, the high haze indicates that more light is scattered; thus there is a degree of balance between the diffraction angle and scattering intensity.
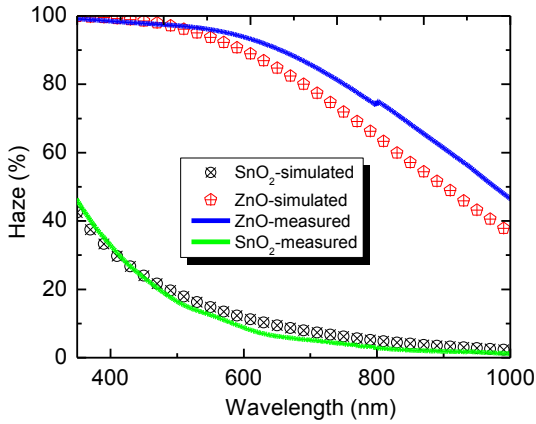
Fig. 6. Simulated and measured values for haze of glass/ZnO:Al, and glass/SnO$_2$:F architectures.

3.2.3. Application in tandem solar cells

In order to compare the effect of these different substrates on the light trapping ability of tandem solar cells, p-i-n type a-Si:H/μc-Si:H tandem solar cells were fabricated employing ZnO:Al and SnO$_2$:F as the front TCO films in the same condition. The EQE curves were also calculated for the two tandem solar cells with different TCOs in order to illustrate the effect of the surface feature sizes on the light absorption of a-Si:H/μc-Si:H tandem solar cell.

Fig. 7 shows a schematic diagram of the a-Si:H/μc-Si:H tandem solar cells that were deposited on SnO$_2$ and ZnO:Al substrates. A subsequent EQE simulation evaluated the contribution of doped layers, such as p and n layers of the sub-cells and back reflectors. For both materials, the physical properties and thickness were kept at the same values for all layers, except for the lateral and vertical feature size of substrates. As shown in Fig. 7, even though the real surface profiles exhibited quite random characteristics, the simulation was based on a simplified surface with 2D triangular textures with a fixed width and height based on the real features shown in Fig. 2. For instance, a triangular unit with a width of 200 nm and height of 35 nm was adopted to simulate the surface morphology of
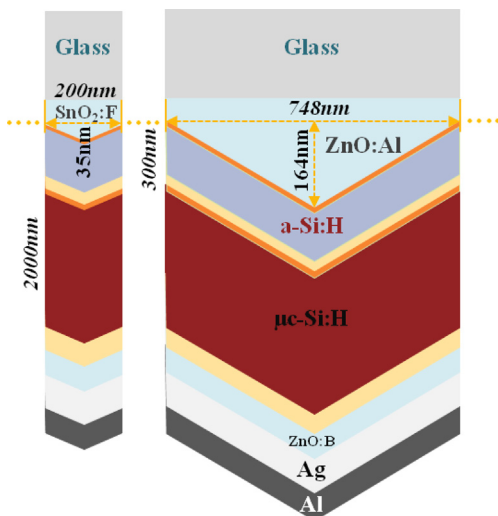
the SnO$_2$ substrate and a width of 748 nm and height of 160 nm were used for the ZnO:Al substrate. An analysis of these layers by an FDTD program [16,22] was used to determine their wave propagation and absorption properties; polarization of the input wave being assumed to be TE wave.

Based on the calculated electric field distribution $E(x,z)$ in the a-Si:H and μc-Si:H intrinsic layers from the FDTD program, the external quantum efficiency EQE can be obtained using the following formula [16]:

$$\text{EQE} = \frac{1}{P_{\text{inp}}} \int \frac{1}{2} c \varepsilon_0 n \alpha |E(x,z)|^2 \mathrm{d}x\, \mathrm{d}z$$

where P_{inp} is the total power incident on the triangular unit cell (1 W in this instance), c is the speed of light in a vacuum, ε_0 is the free space permittivity, n is the refractive index at a given point (x,z), and α is the absorption coefficient.

Fig. 8 shows the measured and simulated EQEs of the two cells, with the derived J_{sc} values presented in Table 1. As shown in Fig. 8a, the combination of magnetron-sputtered and texture-etched ZnO:Al evidently enhances the long-wavelength response, albeit at the expense of its short-wavelength response. As shown in Table 1, the J_{sc} for the experimentally measured cell based on ZnO:Al is 11.25 and 13.89 mA cm^{-2} in the top and bottom cells, respectively. However, for the cell based on a SnO$_2$:F substrate, the J_{sc} of the top cell was 12.46 mA cm^{-2}, whereas the bottom was only 10.61 mA cm^{-2}. Thus, as was discussed in Section 3.2.2, a balance exists between the diffraction angle and scattering intensity that allows ZnO:Al to scatter more light despite being concentrated within a small angular range; its high haze playing a key role in improving its long wavelength response.

The higher J_{sc} of the top cell on SnO$_2$:F results from the nano-features of its surface, which acts as an effective refractive index gradient that reduces reflection and increases the short-wavelength light coupling. As shown in Fig. 8b, the simulated EQE shows a similar trend; and since the size of lateral and vertical features of the substrates was the only variable in this, the variation in the EQE curves between ZnO:Al and SnO$_2$:F clearly shows the result of the differences in their surface feature size. That is, the long-wavelength response of ZnO:Al is attributable to its micro-features, whereas the higher short-wavelength response of SnO$_2$:F comes from its nano-features. From the total EQE curves plotted in Fig. 8c we also can see that the response of ZnO: Al between 750 and 1100 nm is higher than that of SnO$_2$:F, and slightly reduced in the short wavelength region. However, the total current density of ZnO:Al increases significantly in comparison to SnO$_2$:F, both in experiments and simulations (Table 1). Indeed, it has been shown that ZnO:Al performs particularly well in μc-Si: H single junction cells [23].

3.3. Light trapping of the amorphous silicon top cell

As shown in the previous discussion, although ZnO:Al substrate can improve the long-wavelength spectral response effectively, this comes at the expense of the J_{sc} of the top cell. Consequently, there is a need to develop a suitable photon management strategy to increase the absorption in the a-Si:H top cell. The most promising approach is the incorporation of randomly-textured surfaces with a small feature size [15]. In addition, the incorporation of an efficient IR between the top a-Si:H and bottom μc-Si:H cell is an effective means of trapping more light. Such a reflector should have both a low refractive index and high transmittance, so that it can effectively reflect the shorter wavelength portion of the top cell while simultaneously transmit longer wavelength to the bottom cell [24].
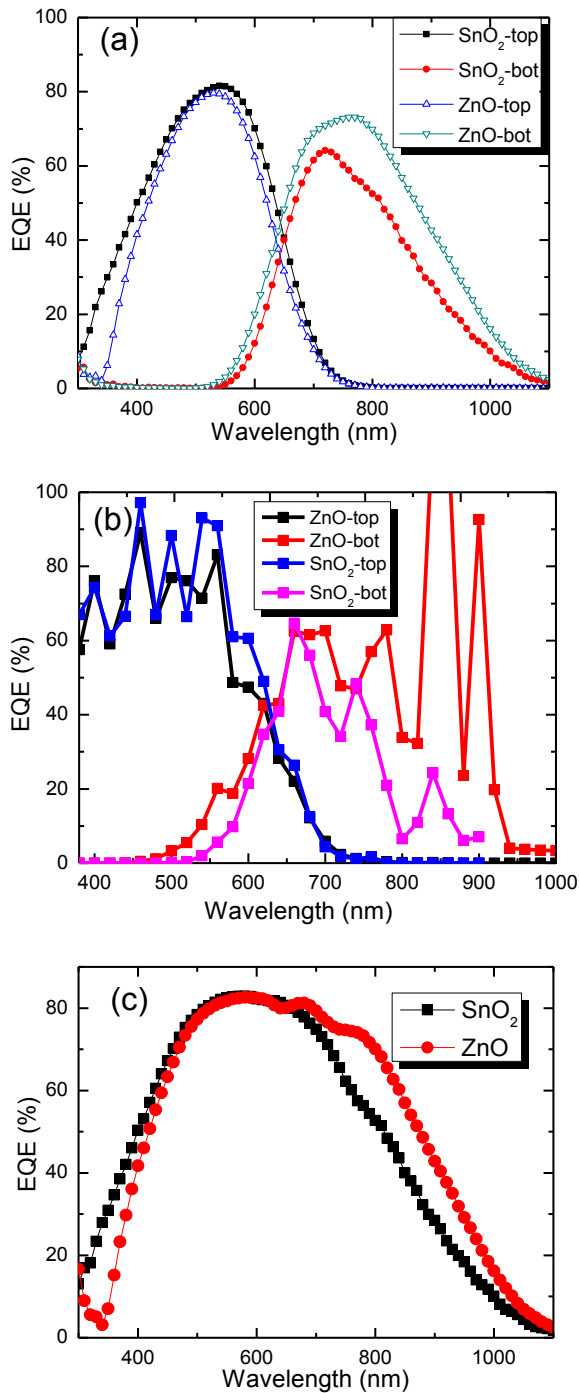

Fig. 7. Schematic diagram of a-Si:H/μc-Si:H tandem solar cells on SnO$_2$:F and ZnO:Al substrates.
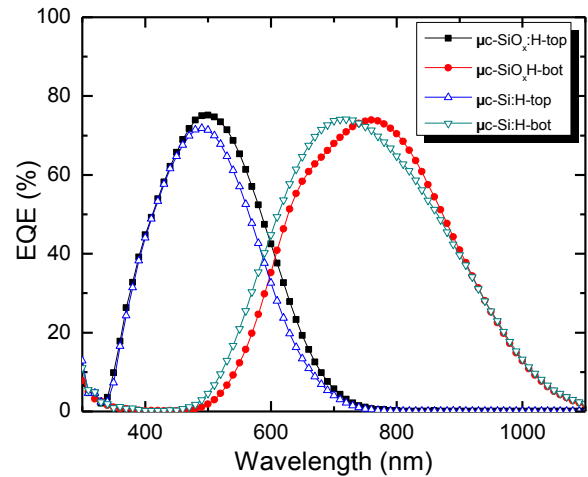
Fig. 9. Experimentally measured EQEs of an a-Si:H/μc-Si:H tandem cell configuration, with and without μc-SiO$_x$:H.

Traditionally, this is achieved by transparent conducting oxides (TCOs) such as doped ZnO [25,26] or n-type silicon oxide (SiO$_x$) materials [27–31]. Doped ZnO, however, tends to form an unintended lateral shunt at the back reflecting metal layer on account of its high conductivity. Another drawback of using TCO-based IR layer is that their deposition and patterning require discontinuous steps undertaken outside the process chamber during the plasma-enhanced chemical vapor deposition (PECVD) of the top and bottom cell layers, whereas SiO$_x$ can be grown directly by PECVD [32–34]. Another significant advantage of SiO$_x$ is that its refractive index and conductivity can be conveniently adjusted by altering the gas flow ratios of CO$_2$/SiH$_4$ and PH$_3$/SiH$_4$ [35].

Fig. 9 shows the EQE of solar cells with and without a μc-SiO$_x$:H reflector, which clearly demonstrates the considerable transfer of absorbed light from the bottom cell to the top cell that this reflector creates in the spectral range between 480 and 720 nm [36]. The amount of current transferred in this instance corresponds to 1.1 mA cm^{-2}, resulting in an increase in J_{sc} from 8.45 and 15.72 mA cm^{-2} to 9.53 and 14.92 mA cm^{-2} for the top and bottom cells, respectively. The improvement in response evident in the spectrum region between 720 and 900 nm when an n-type μc-SiO$_x$:H reflector is inserted is attributed to a reduction in parasitic optical losses.

The J_{sc} for the tandem cells shown in Table 2 demonstrates that by incorporating a μc-SiO$_x$:H reflector, the spectral responses of both subcells are adjusted for the current matching, the spectrum obtains a better distribution and the absorption is enhanced.

In conclusion, the incorporation of IR can reflect the visible light back into the top cell and transmit of the incoming infrared light to the bottom cell. The J_{sc} gain of the top cell can be strongly enhanced with an IR, which reflects, but also scatters the light into the top cell. Although a fraction of the infrared light response of the bottom cell is sacrificed, the visible light response of the top cell is

Fig. 8. (a) Experimentally measured, (b) simulated EQE (c) and total EQE of an a-Si:H/μc-Si:H tandem cell on ZnO:Al and SnO$_2$:F substrates. Corresponding J_{sc}s of the top and bottom cell, as calculated from the EQE in (a), are listed in Table 1.

Table 1
The short circuit current density of experimentally measured and simulated cells that based on different TCOs(AZO and SnO$_2$).

	Cell type	$J_{sc\ top}$(mA cm^{-2})	$J_{sc\ bot}$(mA cm^{-2})	J_{scsum}(mA cm^{-2})
Measured	SnO$_2$	12.46	10.61	23.07
	ZnO	11.25	13.89	25.14
Simulated	SnO$_2$	11.73	6.71	18.44
	ZnO	10.71	11.57	22.28

Table 2
The short circuit current density of experimentally measured a-Si:H/μc-Si:H micromorph tandem cell configuration with μc-SiO$_x$: H.

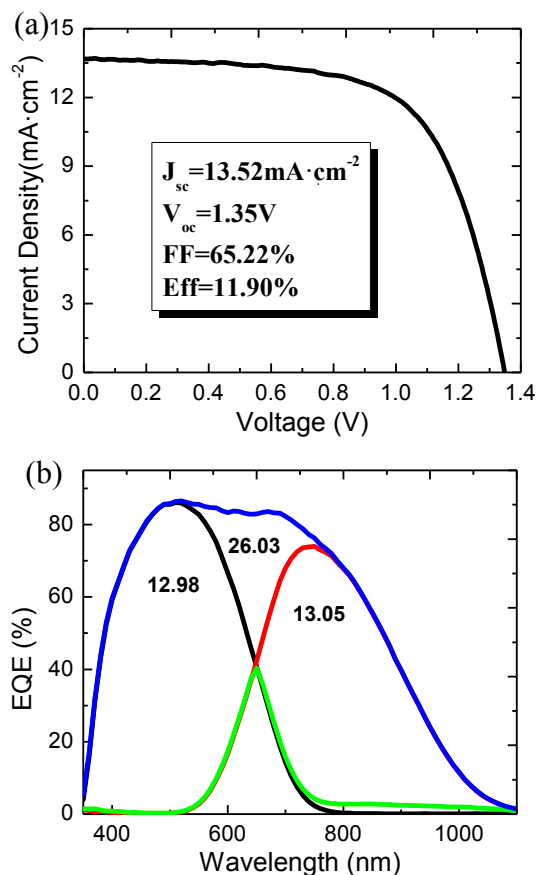| Cell type	$J_{sc\ top}$(mA cm^{-2})	$J_{sc\ bot}$(mA cm^{-2})	$J_{sc\ sum}$(mA cm^{-2})
n type μc-Si:H	8.45	15.72	24.17
n type μc-SiO$_x$:H	9.53	14.92	24.45

Fig. 10. (a) J–V characteristics and (b) EQE of an optimized a-Si:H/μc-Si:H tandem solar cell.

improved with the IR and optimized matching conditions for a tandem cell structure are found.

3.4. The optimized amorphous silicon/microcrystalline silicon tandem cell

From the previous analysis, we have seen that the electrical characteristics and light trapping properties of a front electrode have a great impact on the overall performance of a solar cell. Thus, by further optimizing the surface morphology and adjusting of the deposition process, an efficiency of up to 11.90% (V_{oc} = 1.35 V, J_{sc} = 13.52 mA cm^{-2}, FF = 65.22%) was obtained for an amorphous silicon/microcrystalline silicon tandem cell as shown in Fig. 10.

4. Conclusions

This study has demonstrated that the conversion efficiency of amorphous/microcrystalline silicon tandem solar cells can be improved by varying the light trapping strategies of the top and the bottom cells. The use of magnetron-sputtered and texture-etched ZnO:Al as a front TCO was found to improve the response of the bottom cell and total current density dramatically, but also reduce the J_{sc} of the top cell in comparison to SnO$_2$. To mitigate this effect and produce better current matching, an intermediate reflector (n-SiO$_x$: H) was inserted between the cells and was demonstrated to dramatically improve the top cell's J_{sc}.

References

[1] B. Rech, O. Kluth, T. Repmann, T. Roschek, J. Springer, J. Müller, F. Finger, H. Stiebig, H. Wagner, Sol. Energy Mater. Sol. Cells 74 (2002) 439–447.
[2] M. Vanecek, J. Springer, A. Poruba, O. Kluth, T. Repmann, B. Rech, N. Wyrsch, J. Meier, A. Shah, in: Proceedings of the 3rd WCPEC, Osaka, Japan IEEE, New York, 2003, pp. 1527–1532.
[3] K. Yamamoto, A. Nakajima, M. Yoshimi, T. Sawada, S. Fukuda, T. Suezaki, M. Ichikawa, Y. Koi, M. Goto, T. Meguro, T. Matsuda, M. Kondo, T. Sasaki, Y. Tawada, Sol. Energy 77 (2004) 939–949.
[4] C. Rockstuhl, F. Lederer, T. Beckers, R. Carius, Appl. Phys. Lett. 94 (2009) 211101–211101-3.
[5] J. Krc, K. Brecl, F. Smole, M. Topic, Sol. Energy Mater. Sol. Cells 90 (2006) 3339–3344.
[6] T. Matsui, M. Kondo, A. Matsuda, Jpn. J. Appl. Phys. 42 (2003) L901–L903.
[7] Y. Nakano, S. Goya, T. Watanabe, N. Yamashita, Y. Yonekura, Thin Solid Films 506–507 (2006) 33–37.
[8] J. Muller, B. Rech, J. Springer, M. Vanecek, Solar Energy 77 (2004) 917–930.
[9] R.G. Gordon, MRS Bull. 25 (2000) 52–57.
[10] K. Sato, Y. Gotoh, Y. Wakayama, Y. Hayashi, K. Adachi, H. Nishimura, Rep. Res. Lab. 42 (1992) 129–137. Asahi Glass Co. Ltd.
[11] C. Beneking, B. Rech, S. Wieder, O. Kluth, H. Wagner, W. Frammelsberger, R. Geyer, P. Lechner, H. R€ubel, H. Schade, Thin Solid Films 351 (1999) 241–246.
[12] B. Schroeder, Thin Solid Films 430 (2003) 1–6.
[13] T. Yoshinobu, H. Iwamoto, H. Iwasaki, Jpn. J. Appl. Phys. 33 (1994) 383–387.
[14] S.J. Fang, S. Haplepete, W. Chen, C.R. Helms, Hal Edwards, J. Appl. Phys. 82 (1997) 5891–5898.
[15] U. Palanchoke, V. Jovanov, H. Kurz, R. Dewan, P. Magnus, H. Stiebig, D. Knipp, Appl. Phys. Lett. 102 (2013) 083501-1–083501-3.
[16] R. Dewan, M. Marinkovic, R. Noriega, S. Phadke, A. Salleo, D. Knipp, Opt. Express 17 (2009) 23058–23065.
[17] S. Kim, J.W. Chung, H. Lee, J. Park, Y. Heo, H.M. Lee, Sol. Energy Mater. Sol. Cells 119 (2013) 26–35.
[18] K. Jager, M. Fischer, R.A.M.M. Van Swaaij, M. Zeman, J. Appl. Phys. 111 (2012), 083108–083108-9.
[19] D. Dominé, F.J. Haug, C. Battaglia, C. Ballif, J. Appl. Phys. 107 (2010) 044504–044504-8.
[20] K. Bittkau, M. Schulte, M. Klein, T. Beckers, R. Carius, Thin Solid Films 519 (2011) 6538–6543.
[21] D. Madzharov, R. Dewan, D. Knipp, Opt. Express 19 (2011) A95–A107.
[22] V.E. Ferry, A. Polman, H.A. Atwater, ACS Nano 5 (2011) 10055–10064.
[23] O. Vetterl, F. Finger, R. Carius, P. Hapke, L. Houben, O. Kluth, Sol. Energy Mater. Sol. Cells 62 (2000) 97–108.
[24] S. Jung, B. Kim, M. Shin, Sol. Energy Mater. Sol. Cells 121 (2014) 1–7.
[25] R. Biron, S. Hänni, M. Boccard, C. Pahud, K. Söderström, M. Duchamp, R. Dunin-Borkowski, G. Bugnon, L. Ding, S. Nicolay, G. Parascandolo, F. Meillaud, M. Despeisse, F.J. Haug, C. Ballif, Sol. Energy Mater. Sol. Cells 114 (2013) 147–155.
[26] G. Bugnon, T. Söderström, S. Nicolay, L. Ding, M. Despeisse, A. Hedler, J. Eberhardt, J. Wachtendorf, C. Ballif, Sol. Energy Mater. Sol. Cells 95 (2011) 2161–2166.
[27] D. Domine, P. Buehlmann, J. Bailat, A. Billet, F. Meillaud, A. Feltrin, C. Ballif, Phys. Status Solidi RRL 2 (2008) 163–165.
[28] P. Buehlmann, J. Bailat, D. Domine, A. Billet, F. Meillaud, A. Feltrin, C. Ballif, Appl. Phys. Lett. 91 (2007) 143505-1–143505-3.
[29] T. Grundler, A. Lambertz, F. Finger, Phys. Status Solidi C 7 (2010) 1085–1088.
[30] M. Despeisse, C. Battaglia, M. Boccard, G. Bugnon, M. Charriere, P. Cuony, S. Hänni, L. Lofgren, F. Meillaud, G. Parascandolo, T. Söderström, C. Ballif, Phys. Status Solidi (A) 208 (2011) 1863–1868.
[31] M. Despeisse, G. Gugnon, A. Feltrin, M. Stueckelberger, P. Cuony, F. Meillaud, A. Billet, C. Ballif, Appl. Phys. Lett. 96 (2010) 073507–073507-3.
[32] D. Das, A.K. Barua, Sol. Energy Mater. Sol. Cells 60 (2000) 167–179.
[33] A. Janotta, R. Janssen, M. Schmidt, T. Graf, M. Stutzmann, L. Görgens, A. Bergmaier, G. Dollinger, C. Hammerl, S. Schreiber, B. Stritzker, Phys. Rev. B: Condens. Matter 69 (2004) 11520 6–115206-16.
[34] V. Smirnov, W. Böttler, A. Lambertz, H. Wang, R. Carius, F. Finger, Phys. Status Solidi C 7 (2010) 1053–1056.
[35] D. Das, M. Jana, A.K. Barua, Sol. Energy Mater. Sol. Cells 63 (2000) 285–297.
[36] P. Obermeyer, C. Haase, H. Stiebig, Appl. Phys. Lett. 92 (2008) 181102–181102-3.